




Rare-earth monopnictides: Family of antiferromagnets hosting magnetic Fermi arcsYevhen Kushnirenko ^{1,2}, Benjamin Schruck,¹ Brinda Kuthanazhi,^{1,2} Lin-Lin Wang,¹ Junyeong Ahn,³ Evan O'Leary ^{1,2}, Andrew Eaton,^{1,2} S. L. Bud'ko,^{1,2} Robert-Jan Slager,^{3,4,*} P. C. Canfield,^{1,2,†} and Adam Kaminski ^{1,2,‡}¹*Division of Materials Science and Engineering, Ames Laboratory, Ames, Iowa 50011, USA*²*Department of Physics and Astronomy, Iowa State University, Ames, Iowa 50011, USA*³*Department of Physics, Harvard University, Cambridge, Massachusetts 02138, USA*⁴*TCM Group, Cavendish Laboratory, University of Cambridge, Cambridge CB3 0HE, United Kingdom*

(Received 13 June 2022; accepted 24 August 2022; published 8 September 2022)

Since the discovery of topological insulators a great deal of research effort has been devoted to magnetic topological materials, in which nontrivial spin properties can be controlled by magnetic fields, culminating in a wealth of fundamental phenomena and possible applications. The main focus was on ferromagnetic materials that can host Weyl fermions and therefore spin-textured Fermi arcs. The recent discovery of Fermi arcs and new magnetic band splitting in the antiferromagnet (AFM) NdBi has opened up new avenues for exploration. Here we show that these uncharted effects are not restricted to this specific compound, but also emerge in CeBi and NdSb when they undergo paramagnetic to AFM transition. Our data show that the Fermi arcs in NdSb have twofold symmetry, leading to strong anisotropy that may enhance effects of spin textures on transport properties. Our findings thus demonstrate that the RBi and RSb series are materials that host magnetic Fermi arcs and may be a potential platform for modern spintronics.

DOI: [10.1103/PhysRevB.106.115112](https://doi.org/10.1103/PhysRevB.106.115112)**I. INTRODUCTION**

Many of the rare-earth monopnictides RBi and RSb (where R is a rare-earth element) [1–8] exhibit an antiferromagnetic (AFM) transition at low temperatures. Some members of this family such as CeSb and CeBi exhibit complex evolution of electronic structure as they undergo a cascade of AFM transitions upon cooling. These transitions were previously reported in measurements of magnetization and resistivity [9], specific heat [10], neutron diffraction [11,12], and angle-resolved photoemission spectroscopy (ARPES) [13]. Recently, the existence of various types of topologically nontrivial states [14–16], including Weyl semimetals, were predicted to occur in several of these compounds [17–20]. Weyl semimetals and, as a consequence, Fermi arcs that connect a pair of Weyl points were predicted to occur in ferromagnetically ordered CeBi, CeSb, and GdBi [18,19,21]. There are some experiments that seem to support this hypothesis: signatures of Weyl fermions were reported by transport measurements [18] and scanning tunneling spectroscopy measurements [22]. However, the ferromagnetic phase of these materials can only be induced by application of an external magnetic field, while in the absence of the field, these materials order only antiferromagnetically.

Since Weyl semimetals can be realized only in systems with either broken time-reversal or inversion symmetry, Fermi arcs are not expected to occur in simple AFM-ordered phases

such as those that were reported to occur in monopnictides by neutron diffraction experiments [1,2,23]. In simple AFM phases, both symmetries are preserved, where a nonsymmorphic time-reversal symmetry has the same role as the time-reversal symmetry. In order for an AFM to realize a Weyl semimetal, it has to have a noncollinear AFM order that does not have nonsymmorphic time-reversal symmetry as in pyrochlore iridates [24]. On the other hand, a recent ARPES study on NdBi [25] has shown that Fermi surface arcs emerge in the AFM phase in this material and undergo unconventional magnetic band splitting upon cooling below T_N . The resulting dispersions are spin textured as demonstrated by recent density functional theory (DFT) calculations [26]. DFT has shown that such Fermi surface arcs exists as a result of noncollinear AFM order with multiple wave vectors (multi- q) as in $2q$ and $3q$. In order to study how the appearance and splitting of these arcs depend on the rare-earth element as well as pnictide element we have extended our ARPES studies to RBi for $R = \text{Ce, Nd, Sm}$ as well as to NdSb. We find that Fermi arcs exist in several members of this NaCl structural family.

II. EXPERIMENTAL DETAILS

Single crystals of CeBi, NdBi, and SmBi were grown out of In flux. The elements with an initial stoichiometry of $R_4\text{Bi}_4\text{In}_{96}$ ($R = \text{Ce, Nd, Sm}$) were put into a fritted alumina crucible [27] and sealed in a fused silica tube under partial pressure of argon. NdSb crystals were grown out of Sn flux using an initial concentration of $\text{Nd}_4\text{Sb}_4\text{Sn}_{96}$. The prepared ampules were heated up to 1100°C over 4 hours and held there for 5 hours. This was followed by a slow cooling to the decanting temperature over 100 hours and decanting of the

* rjs269@cam.ac.uk

† canfield@ameslab.gov

‡ Corresponding author: kaminski@ameslab.gov

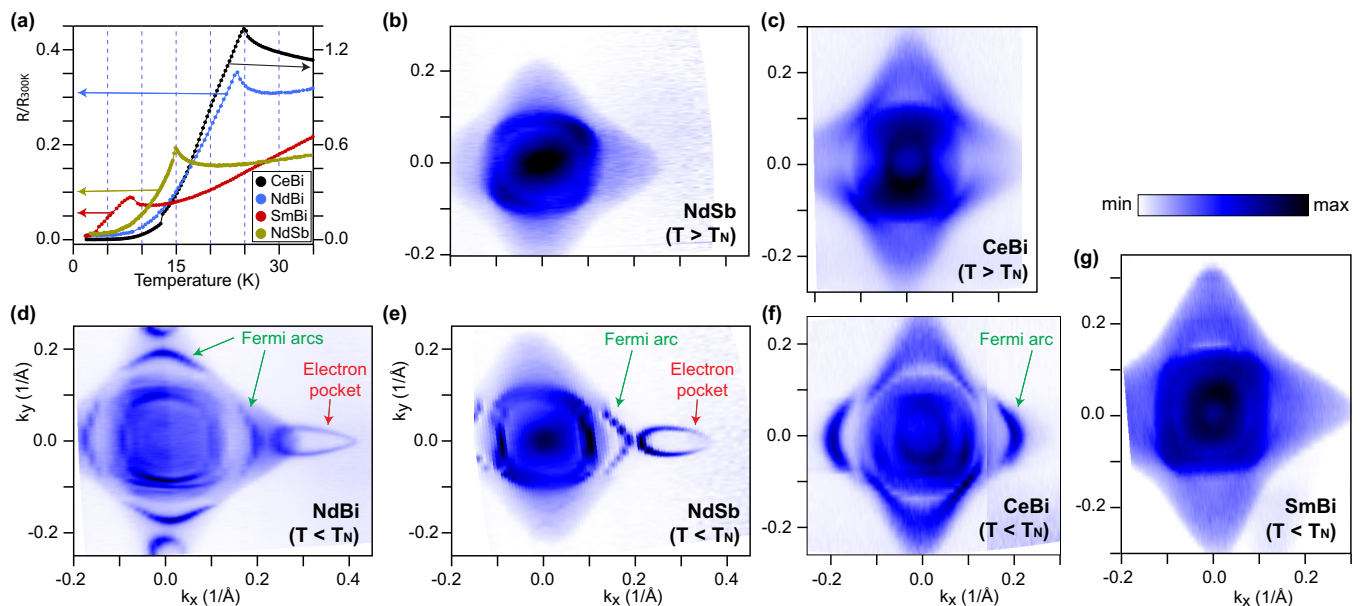


FIG. 1. Resistivity data and Fermi surface maps in paramagnetic and AFM state. (a) Temperature dependence of resistivity for CeBi, NdBi, SmBi, and NdSb normalized by value at 300 K. (b) Fermi surface maps of NdBi measured at $T = 16$ K, in the paramagnetic state. (c) Fermi surface maps of CeBi measured at $T = 30$ K, in the paramagnetic state. (d) and (e) Fermi surface maps of NdBi and NdSb, respectively, measured in the AFM state ($T = 6$ K). (f) Fermi surface maps of CeBi in the AFM state ($T = 13.5$ K). (g) Fermi surface maps of SmBi in the AFM state ($T = 5$ K).

excess flux using a centrifuge [28]. The decanting temperatures were 850°C for CeBi, 700°C for NdBi, and 800°C for both SmBi and NdSb. The cubic crystals obtained were stored and handled in a glove box under nitrogen atmosphere.

ARPES data were collected using a vacuum ultraviolet (VUV) laser ARPES spectrometer that consists of a Scienta DA30 electron analyzer, picosecond Ti:sapphire oscillator, and fourth-harmonic generator [29]. Data from the laser-based ARPES were collected with 6.7 eV photon energy. Angular resolution was set at $\sim 0.1^\circ$ and 1° , along and perpendicular to the direction of the analyzer slit, respectively, and the energy resolution was set at 2 meV. The VUV laser beam was set to vertical polarization. The diameter of the photon beam on the sample was $\sim 15 \mu\text{m}$. Samples were cleaved *in situ* along the (001) plane, usually producing very flat, mirror-like surfaces. The measurements were performed at a base pressure lower than 2×10^{-11} Torr. Results were reproduced using several different single crystals of each material, and extensive temperature cycling.

III. RESULTS AND DISCUSSION

Figure 1(a) shows the temperature dependence of electrical resistivity of CeBi, SmBi, NdBi, and NdSb. All curves demonstrate similar behavior: there is a high-temperature region where resistivity changes gradually, followed by a peak and a rapid decrease upon cooling. Such behavior is associated with loss of spin disorder during the AFM transition. Thermodynamic and transport data identify the following, zero applied magnetic field transition temperatures: $T_N = 25$ K for CeBi, $T_N = 24$ K for NdBi, $T_N = 15$ K for NdSb, and $T_N = 9$ K for SmBi [2,30,31]. These are in agreement with results from other experimental techniques: scanning tunneling

microscopy with a magnetic tip [22] and neutron scattering [1,2,11,12,23]. Whereas the NdBi and NdSb have only a single magnetic phase transition from the paramagnetic phase to the AFM state, the CeBi resistivity data show a second feature at 12.5 K. It is associated with a first-order transition to a different, low-temperature AFM phase. A similar situation occurs in SmBi, which also displays a lower-temperature AFM phase below 7 K [31]. In this study, for CeBi, NdBi, and NdSb, we will focus on the first AFM phase below T_N . For SmBi, where the second transition is only 2 K below T_N , we collected the data at 5 K to ensure we are sufficiently below T_N .

A. Fermi surface maps

We compare the Fermi surface (FS) maps measured by ARPES in the paramagnetic and first AFM states below T_N (except for SmBi, where measurements were done in the second AFM state below T_N) in Figs. 1(b)–1(g). The Fermi surfaces of NdSb and CeBi above T_N , shown in Figs. 1(b) and 1(c), are very similar to each other and are in good agreement with nonmagnetic DFT calculations [17,19,22]. The observed broad features are the result of the 3D projection of dispersing bulk bands onto the k_x , k_y plane of the Brillouin zone (BZ). In the AFM state however, new sharp features appear on the Fermi surface maps [Figs. 1(e) and 1(f)], noticeably similar to the previously observed NdBi elliptical, electron-like pockets located near the tips of the bulk FS [Fig. 1(d)]. Another very interesting feature that emerges is a set of four disconnected contours located near the new electron-like pockets.

The Fermi surface of CeBi in the AFM state [see Fig. 1(f)] also demonstrates disconnected arcs very similar to those

observed in NdBi and NdSb. However, there are no signs of the elliptical pockets on the map. The Fermi arcs present in NdSb and CeBi are twofold symmetric (C_2), while in NdBi they have fourfold (C_4) symmetry. This would be consistent with $2q$ magnetic ordering [26], as signal from the (001) surface would be fourfold symmetric and signal from the (100) or (010) surface would be twofold symmetric. It is also possible that ARPES signal for NdSb and CeBi was originating from a single (010)/(100) domain, while in the NdBi case it was averaged over several domains that were smaller than the size of the laser photon beam ($15 \mu\text{m}$). (See further discussion in Appendix A.)

Despite the fact that DFT calculations [26] for multi- q ordering reproduce experimental surface state features quite well and predict the existence of topological states in this material, according to these calculations, neither the Weyl states in AFM3 q nor the Dirac states in AFM2 q are the sources for the experimentally observed Fermi arcs. Thus these arcs are different from Weyl arcs [32–36].

The data from SmBi measured even at the lowest magnetically ordered phase does not show any additional features in the FS [Fig. 1(g)] in contrast to CeBi, NdBi, and NdSb. Its Fermi surface demonstrates only broad bulk features and similar to the PM state of the other materials. More data are shown in Appendix C.

B. Band dispersion of surface states

For the further analysis of the new states, we measured detailed data sets for the parts of the BZ where they are located. Figure 2(a) shows constant-energy maps for NdSb. The elliptical pocket decreases in size and then disappears at higher binding energies indicating electron-like behavior. This behavior can also be seen from the cuts in Fig. 2(b). The feature identified earlier as an arc moves out to higher k_x values but remains an isolated arc and does not form closed pockets. At the same time the arc feature moves out to higher k_y , essentially covering some of the region the elliptical feature had occupied. The discontinuity of this dispersion is even better seen in the cuts in Fig. 2(b). For example, in cut 2, there are no signs of additional sharp dispersion. Slightly farther away from the Γ point, in cut 3, the dispersion associated with the new surface states begins to appear. Its top is still above the E_F and is therefore not visible in ARPES at these low temperatures. Even farther away, the band moves lower in energy, and we can see its top. In the same cut, another band with electron-like dispersion appears. In all cuts, the lower dispersion exists in a finite momentum range and has sharp cutoffs indicating its arc character.

We performed a similar analysis for the new surface states present in NdBi. Figures 2(c) and 2(d) show constant-energy maps and the dispersion along selected cuts. There is a striking resemblance between surface state features in both materials. The elliptical pockets in NdBi also have an electron-like character. However, the band which forms them is deeper, and therefore the pockets are slightly larger. The hole-like Fermi arcs are clearly visible in these data as the sharp band exists only in a finite momentum range. Thus, the difference between NdBi and NdSb is only quantitative and not qualitative. Please note that the cuts in the NdSb are slightly skewed due

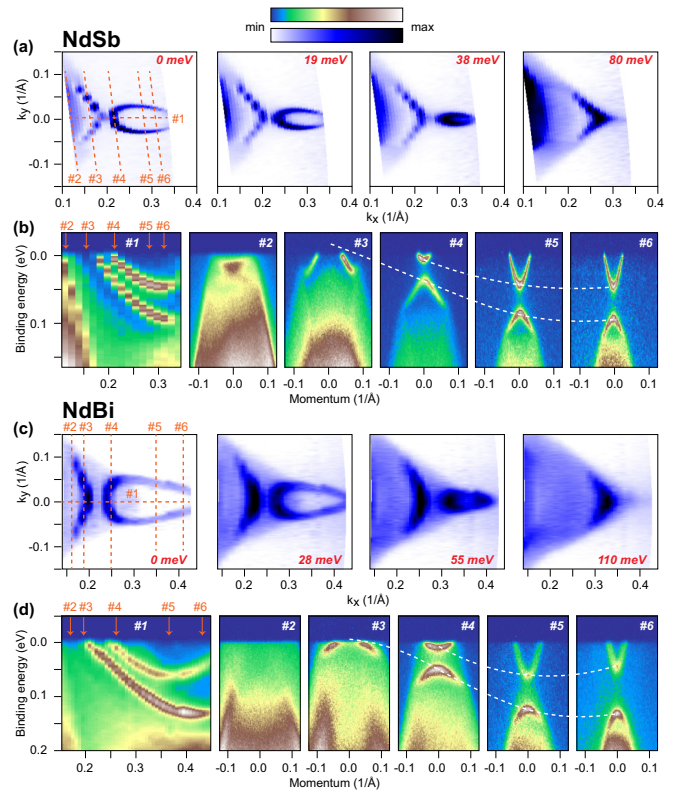


FIG. 2. Dispersion of the surface states in NdSb and NdBi in the AFM state. (a) Constant-energy map for NdSb at binding energies from 0 to 80 meV measured at $T = 6$ K. (b) Band dispersion along the cuts marked with the dashed line in (a). The locations of cuts 2–6 are also marked with the arrows in cut 1. (c) Constant-energy map for NdBi at binding energies from 0 to 110 meV measured at $T = 6$ K. (d) Band dispersion along the cuts marked with the dashed line in (c). The locations of cuts 2–6 are also marked with the arrows in cut 1. The white dashed lines in (b) and (d) are a guide to the eye of location of top and bottom of the hole- and electron-like surface bands and reflect dispersion of the surface states seen in the corresponding cuts 1.

to small angular misalignment of the sample during measurements.

The data for CeBi are presented in Fig. 3(a), where we show the zoomed-in part of the map from Fig. 1(f) and several additional equal-energy plots extracted from the same data set. In Fig. 3(b), we show a different data set which represents measurement on a different domain that has orthogonal orientation of the surface states. The very similar shape of the Fermi contours for two orthogonal domains indicates that the influence of matrix elements is insignificant, and both maps are adequate representations of the Fermi surface of CeBi. These maps demonstrate that arcs evolve with binding energy in a manner similar to two other materials. However, the surface electron pocket that is observed in NdBi and NdSb is absent here, most likely due to much weaker band splitting. Analysis of dispersions along cuts in certain directions reveals more details. Cut 4 in Fig. 3(c) shows that the dispersion which produces the arc (marked with a white arrow) actually consists of two dispersions that are clearly split below 50 meV (see black arrows). The upper dispersion quickly loses its

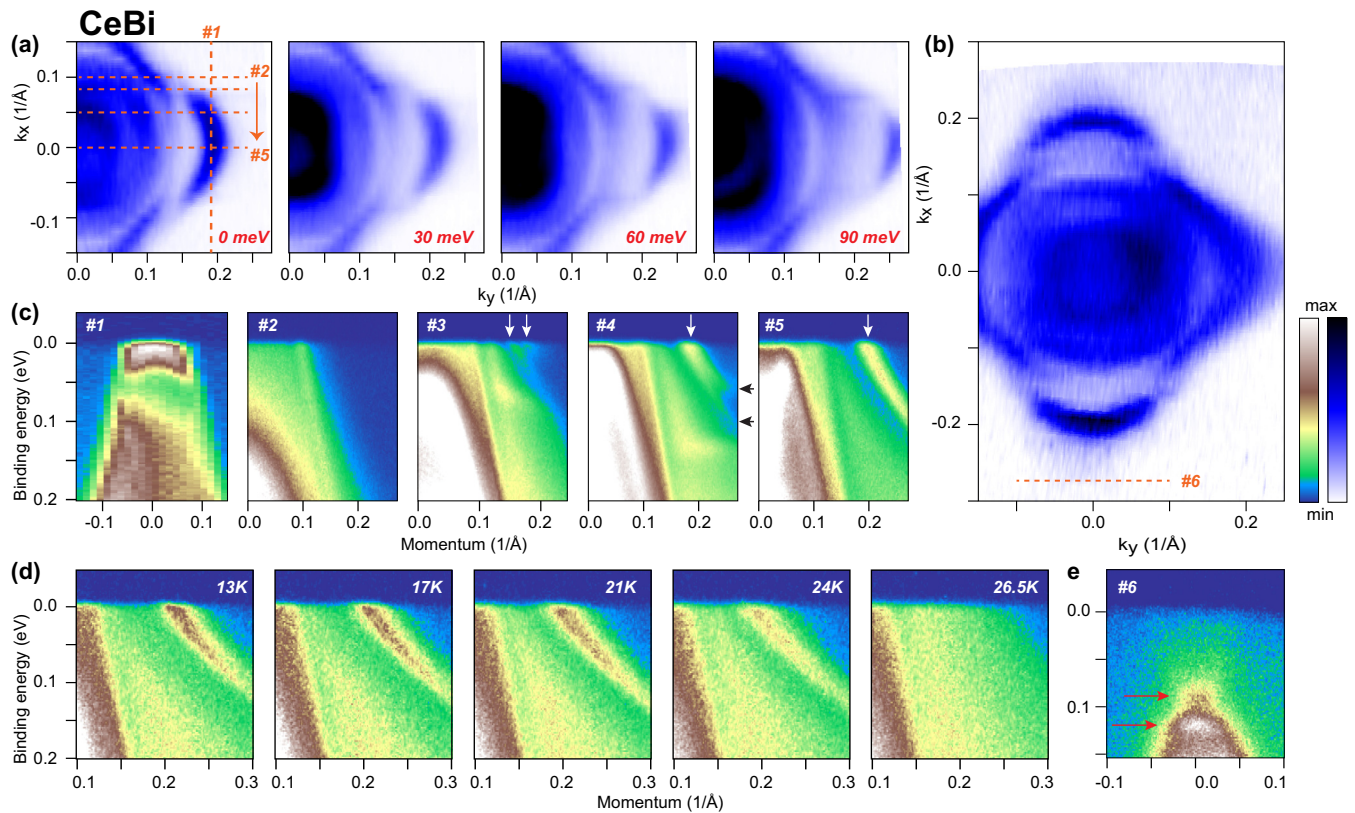


FIG. 3. Dispersion of the surface states in CeBi in the first magnetically ordered state (AFM1) at $T = 13.5$ K. (a) Constant-energy plots at binding energies from 0 to 90 meV. (b) Fermi surface map for a domain with different orientation of magnetic ordering. (c) Band dispersion along the directions marked with the dashed lines in (a). Here, white arrows indicate the location of the surface state dispersions. (d) Temperature dependence of the band dispersion along cut 5 in (a). (e) Band dispersion along the directions marked with the dashed line in (b).

intensity and it becomes difficult to track its behavior beyond that point. If we move closer to the Γ -X cut (cut 5), these two dispersions merge and become indistinguishable. For the opposite direction, the upper band quickly moves higher in energy, and in cut 3, only the bottom of this band is present. Even farther, at cut 2, both surface bands disappear, which again proves the arc character of at least the lower energy branch. However, the upper dispersion does not seem to have an arc character. Most likely, it is not present in cut 2 because, in this part of the BZ, it is located above the Fermi level. We should note that the sharp dispersion in cut 2 is related to the bulk states and is present in the PM states as well (see Appendix B). The presence of two dispersions located close to each other can also explain why the arcs on the Fermi surface of CeBi are thicker than the arcs in NdBi and NdSb. This is better seen in Fig. 1, where all maps are plotted on the same scale. While we see Fermi arcs in both NdBi and NdSb, the arcs we find in CeBi are not present in CeSb [13].

C. Temperature evolution of surface states

The temperature evolution of surface states in CeBi across the AFM transition is shown in Fig. 3(d). The spectrum on the right was measured at $T = 26.5$ K, which corresponds to the paramagnetic state and reveals no traces of the surface states with only broad 3D bands being present. At 24 K the surface

states are already clearly seen. This result is in agreement with $T_N = 25$ K obtained from our resistivity measurements and other methods. Upon further cooling down to 13 K, intensity of the surface states increases. We limit the lower temperature to 13 K in order to compare temperature-dependent data in the initial AFM-ordered state upon cooling from the paramagnetic state.

We compare the temperature evolution of the surface states for NdSb and NdBi in Fig. 4. The Fermi surface maps measured at several different temperatures are shown in panels (a) and (d), horizontal cuts in panels (b) and (e), and vertical cuts in panels (c) and (f), respectively. The Fermi surface maps for both NdSb and NdBi [Figs. 4(a) and 4(d)] show that the separation between electron-like pockets and hole-like Fermi arcs decreases with increased temperature. At the same time, the intensity of the electron-like pocket decreases. Similar behavior is seen in band dispersion plots shown in Fig. 4, panels (b), (c), (e), and (f). At lowest temperature the hole and electron bands are well separated. This separation decreases upon increasing temperature, with the electron band changing its energy more than the hole band. At temperature close to the transition temperature, both bands merge along the horizontal cut, while the intensity of the electron band becomes very weak. Finally, at $T = 15.5$ K for NdSb and 25 K for NdBi, all features associated with the surface state disappear in both Fermi surface maps and dispersion.

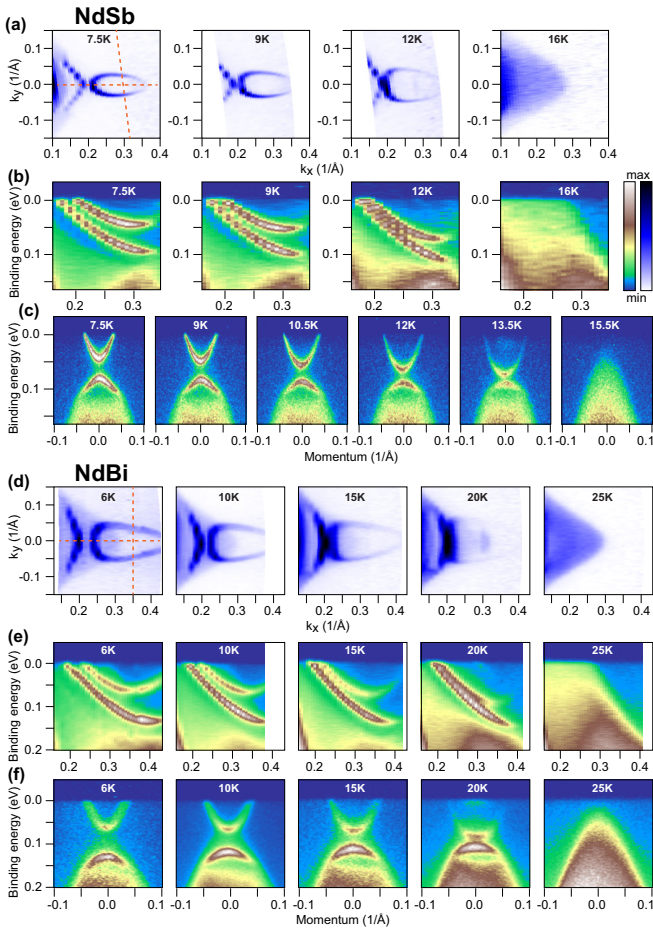


FIG. 4. Temperature evolution of the surface state dispersion for NdSb and NdBi. (a) Fermi surface map of NdSb at four temperatures below and one above T_N . (b) and (c) Band dispersion along directions marked with the horizontal and vertical dashed line in (a), respectively. (d) Fermi surface map of NdBi at five temperatures below and one above T_N . (e) and (f) Band dispersion along directions marked with the horizontal and vertical dashed line in (d), respectively.

The comparison of data measured at similar effective temperatures $T_{eff} = (T/T_N)$ reveals significant differences between CeBi and NdBi/NdSb. For example, the surface state bands in NdSb at 9 K ($T_{eff} = 0.7$) and NdBi at 15 K ($T_{eff} = 0.6$) shown in Fig. 4(e) are already substantially split, while in CeBi, at the lowest temperature shown in Figs. 3(c) and 3(d) (i.e., for even lower $T_{eff} = 0.54$), the splitting is much smaller and visible only in certain cuts. One would have to compare the NdBi data measured at 20 K with CeBi data measured at 13 K to find some similarity. In NdBi at $T = 20$ K, the arc merges with a part of the electron pocket, forming one broad feature on the Fermi surface similar to one observed in CeBi. At the same time, the rest of the electron pocket tends to lose all its intensity at high temperatures. Also, the behavior of the surface state dispersions on the high-temperature spectrum in Fig. 4(e) is reminiscent of the behavior in Fig. 3(c), cut 4, while the high-temperature spectrum in Fig. 4(f) is similar to Fig. 3(e). The spectrum measured at $T = 20$ K in NdBi shows that the bottom of the electron dispersion is drastically more intense than the rest of it. In CeBi, we see a similar

situation: above the band associated with the arc, we see an additional feature, which we associate with the bottom of the electron dispersion. All these similarities indicate that in CeBi, electron-like surface state (SS) dispersion is indeed present, but it is not fully developed due to much smaller splitting. This is likely due to weaker effective magnetic moment. Furthermore, the first-order transition to a different AFM phase that occurs at 12.5 K prevents full formation of this feature that is expected to occur at lower temperatures, as it occurs in NdBi and NdSb.

IV. CONCLUSIONS

In this work, we show that the exciting novel breakthrough features discovered in NdBi, such as spontaneous Fermi surface generation and anomalous magnetic splitting effects that culminate in effective manipulable Fermi arcs, are not restricted to that specific compound. Rather they point to a general and uncharted mechanism that follows a definitive trend over a wide range of monopnictide family members when they undergo AFM transitions. This trend, in terms of relative intensity of the Fermi arcs and energy separation of the magnetic band splitting, seems to scale with the magnetic moments of the rare-earth elements, with Nd having the largest magnetic moment and strongest effects among the compounds we studied. Sm has the smallest magnetic moment with SmBi not exhibiting Fermi arcs or splitting. Ce with its magnetic moment in between exhibits modest Fermi arcs and very small magnetic splitting. As such our results not only set a benchmark for the investigation of novel magnetic surface states in an experimentally accessible class of materials, but open the possibility that other antiferromagnets can also host similar spin-textured Fermi arcs and magnetic splitting.

ACKNOWLEDGMENTS

ARPES measurements were supported by the U.S. Department of Energy, Office of Basic Energy Sciences, Division of Materials Science and Engineering. Ames Laboratory is operated for the U.S. Department of Energy by Iowa State University under Contract No. DE-AC02-07CH11358. Crystal growth and characterization were supported by the Center for the Advancement of Topological Semimetals (CATS), an Energy Frontier Research Center funded by the U.S. DOE, Office of Basic Energy Sciences. R.-J.S. acknowledges funding from Trinity College at the University of Cambridge. J.A. was supported by CATS.

APPENDIX A: DOMAINS IN NdSb AND NbBi

In Fig. 5, we show one more Fermi surface map of NdSb measured in the AFM state. In this map, one can see the same arc features and ellipse pockets as in Fig. 1(d). However, in contrast to Fig. 1(d), here, they are present in both horizontal and vertical directions. Since both maps were measured with the same (linearly vertically polarized) light, the almost complete absence of the SS features along the vertical direction in Fig. 1(e) cannot be a result of the matrix elements. Most likely, the surface states are visible along vertical and horizontal directions in Fig. 5 due to the presence of domains. That

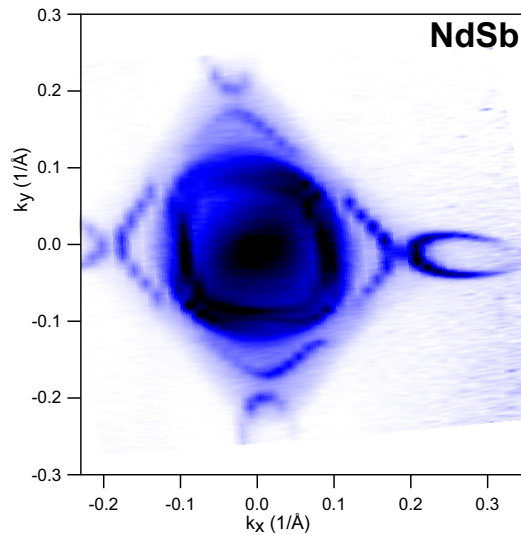


FIG. 5. Fermi surface map of NdSb that is a superposition of signals from domains of different orientations.

would imply that the domain size in NdSb is smaller than our laser beam ($\sim 15 \mu\text{m}$) and the photoelectron intensity is therefore a superposition of signal from several domains that have SS oriented along vertical and horizontal directions.

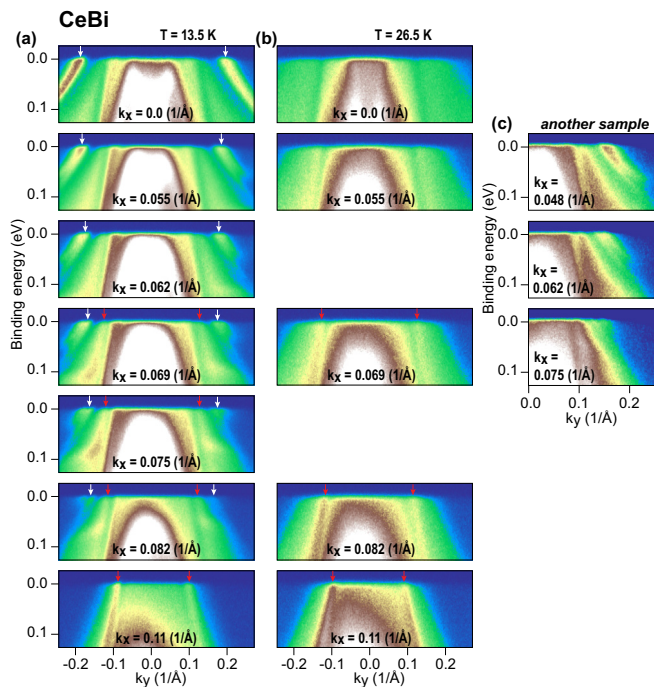


FIG. 6. Band dispersion in the AFM and PM states of CeBi. (a) Band dispersions along several cuts parallel to the Γ -X direction measured in the AFM state. Here, white and red arrows indicate the location of the surface state and bulk dispersions, respectively. (b) The same band dispersions as in (a) but measured in the PM state. (c) Band dispersions measured in the AFM state from another sample.

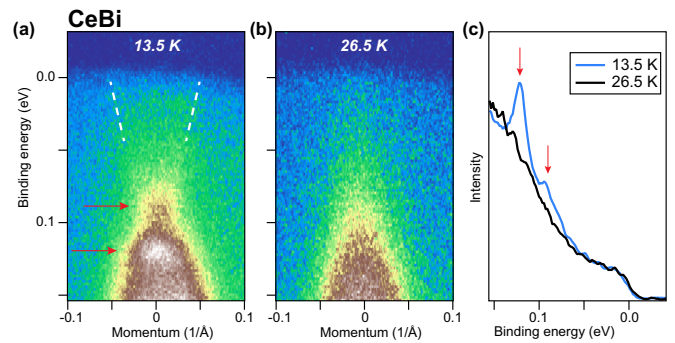


FIG. 7. Band dispersion below and above T_N in CeBi. (a) Spectrum measured in the AFM state [the same as Fig. 3(e)]. (b) The same spectrum as in (a) but measured in the PM state. (c) Energy distribution curves taken through the band center from (a) and (b).

APPENDIX B: ADDITIONAL DATA: CeBi

In the left column of Fig. 6, we show cuts from Fig. 3(c) in a wider momentum range and several more cuts obtained from the same data set. For comparison in the right column, we plot corresponding cuts obtained from the data set measured in the PM state. The presence of two SS dispersions is seen on both sides of the low-temperature plots. The marginal asymmetry of these plots is caused by a slight misalignment of the sample. Different shapes of the lower and upper SS dispersion indicate that the observed splitting is real but not a result of detecting signal from two sample crystallites. This conclusion is confirmed by observing two SS dispersions in the data obtained from two other samples: Fig. 6(c) and Fig. 7(a).

Besides SS dispersions (marked with white arrows), low-temperature plots display another sharp feature (marked with red arrows). However, in contrast to the unconventional SS, this dispersion is also seen in the data measured in the PM phase [second column of Fig. 6(b)]. It is formed by the bulk states and forms a part of the outer pocket around the Γ point.

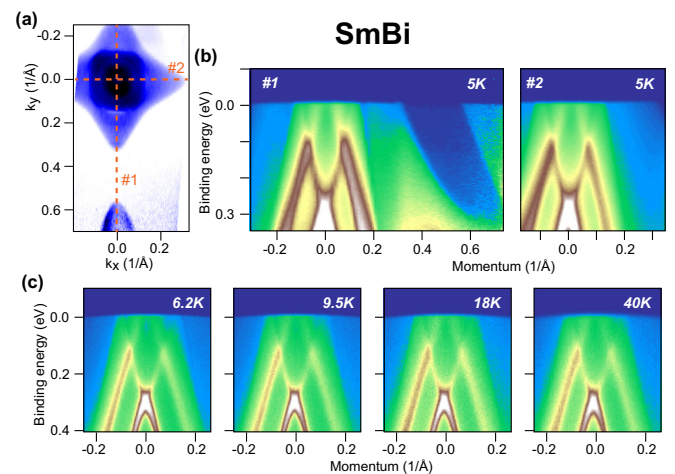


FIG. 8. Additional data from SmBi. (a) Fermi surface of SmBi in the AFM state [the same as Fig. 1(f)]. (b) Band dispersions along the directions marked with the dashed line in (a). (c) Temperature dependence of the band dispersions along Γ -X direction.

In Figs. 7(a) and 7(b), we show the spectrum from Fig. 3(e) and a corresponding spectrum measured in the PM state. In the PM state, we observe only one wide blob of intensity associated with bulk states. In the AFM state, two additional features appear. This is even better seen from the energy distribution curves taken through the band center [see Fig. 7(c)]. Here, the 26.5 K curve shows a smooth background of the bulk states, and the 13.5 K curve shows two pronounced peaks on this background. This result, together with the similarity of Fig. 7(a) and Fig. 4(f) (20 K), confirms that these features are associated with two unconventional surface states.

APPENDIX C: ADDITIONAL DATA: SmBi

In Fig. 8(b), we show two orthogonal cuts that represent the Γ -X direction obtained from the same data set as the Fermi surface map in Fig. 1(f). In contrast to similar cuts for three other materials [see Figs. 2(b), cut 1, and 2(d), cut 1, and Fig. 3(d)], these cuts do not show the presence of any signs of sharp surface states. A spectrum measured along Γ -X of another sample down to 6.2 K [Fig. 8(c)] also does not indicate the presence of these states and does not qualitatively change with increasing temperature above T_N .

- [1] N. Nereson and G. Arnold, *J. Appl. Phys.* **42**, 1625 (1971).
- [2] H. Bartholin, P. Burlet, S. Quezel, J. Rossat-Mignod, and O. Vogt, *J. Phys., Colloq.* **40**, C5-130 (1979).
- [3] P. C. Canfield and Z. Fisk, *Philos. Mag. B* **65**, 1117 (1992).
- [4] H. Kumigashira, S.-H. Yang, T. Yokoya, A. Chainani, T. Takahashi, A. Uesawa, T. Suzuki, O. Sakai, and Y. Kaneta, *Phys. Rev. B* **54**, 9341 (1996).
- [5] P. C. Canfield and I. R. Fisher, *J. Cryst. Growth* **225**, 155 (2001).
- [6] Y. Wu, Y. Lee, T. Kong, D.-x. Mou, R. Jiang, L. Huang, S. L. Bud'ko, P. C. Canfield, and A. Kaminski, *Phys. Rev. B* **96**, 035134 (2017).
- [7] K. Kuroda, M. Ochi, H. S. Suzuki, M. Hirayama, M. Nakayama, R. Noguchi, C. Bareille, S. Akebi, S. Kunisada, T. Muro, M. D. Watson, H. Kitazawa, Y. Haga, T. K. Kim, M. Hoesch, S. Shin, R. Arita, and T. Kondo, *Phys. Rev. Lett.* **120**, 086402 (2018).
- [8] A. P. Sakhya, B. Wang, F. Kabir, C.-Y. Huang, M. M. Hosen, B. Singh, S. Regmi, G. Dhakal, K. Dimitri, M. Sprague, R. Smith, E. D. Bauer, F. Ronning, A. Bansil, and M. Neupane, [arXiv:2203.05879](https://arxiv.org/abs/2203.05879).
- [9] T. A. Wiener and P. C. Canfield, *J. Alloys Compd.* **303**, 505 (2000).
- [10] J. Rossat-Mignod, P. Burlet, H. Bartholin, O. Vogt, and R. Lagnier, *J. Phys. C* **13**, 6381 (1980).
- [11] N. Nereson and V. Struebing, *AIP Conf. Proc.* **5**, 1385 (1972).
- [12] P. Schobinger-Papamantellos, P. Fischer, O. Vogt, and E. Kaldis, *J. Phys. C* **6**, 725 (1973).
- [13] K. Kuroda, Y. Arai, N. Rezaei, S. Kunisada, S. Sakuragi, M. Alaei, Y. Kinoshita, C. Bareille, R. Noguchi, M. Nakayama, S. Akebi, M. Sakano, K. Kawaguchi, M. Arita, S. Ideta, K. Tanaka, H. Kitazawa, K. Okazaki, M. Tokunaga, Y. Haga, S. Shin, H. S. Suzuki, R. Arita, and T. Kondo, *Nat. Commun.* **11**, 2888 (2020).
- [14] H. Watanabe, H. C. Po, and A. Vishwanath, *Sci. Adv.* **4**, eaat8685 (2018).
- [15] A. Bouhon, G. F. Lange, and R.-J. Slager, *Phys. Rev. B* **103**, 245127 (2021).
- [16] L. Elcoro, B. J. Wieder, Z. Song, Y. Xu, B. Bradlyn, and B. A. Bernevig, *Nat. Commun.* **12**, 5965 (2021).
- [17] Xu Duan, F. Wu, J. Chen, P. Zhang, Y. Liu, H. Yuan, and C. Cao, *Commun. Phys.* **1**, 71 (2018).
- [18] C. Guo, C. Cao, M. Smidman, F. Wu, Y. Zhang, F. Steglich, F.-C. Zhang, and H. Yuan, *npj Quantum Mater.* **2**, 39 (2017).
- [19] Z. Huang, C. Lane, C. Cao, G.-X. Zhi, Y. Liu, C. E. Matt, B. Kuthanazhi, P. C. Canfield, D. Yarotski, A. J. Taylor, and J.-X. Zhu, *Phys. Rev. B* **102**, 235167 (2020).
- [20] Y. Fang, F. Tang, Y. R. Ruan, J. M. Zhang, H. Zhang, H. Gu, W. Y. Zhao, Z. D. Han, W. Tian, B. Qian, X. F. Jiang, X. M. Zhang, and X. Ke, *Phys. Rev. B* **101**, 094424 (2020).
- [21] Z. Li, D.-D. Xu, S.-Y. Ning, H. Su, T. Itaka, T. Tohyama, and J.-X. Zhang, *Int. J. Mod. Phys. B* **31**, 1750217 (2017).
- [22] C. E. Matt, Y. Liu, H. Pirie, N. C. Drucker, N. H. Jo, B. Kuthanazhi, Z. Huang, C. Lane, J.-X. Zhu, P. C. Canfield, and J. E. Hoffman, *Phys. Rev. B* **105**, 085134 (2022).
- [23] P. Manfrinetti, A. Provino, A. Morozkin, and O. Isnard, *J. Alloys Compd.* **487**, L28 (2009).
- [24] X. Wan, A. M. Turner, A. Vishwanath, and S. Y. Savrasov, *Phys. Rev. B* **83**, 205101 (2011).
- [25] B. Schruck, Y. Kushnirenko, B. Kuthanazhi, J. Ahn, L.-L. Wang, E. O'Leary, K. Lee, A. Eaton, A. Fedorov, R. Lou, V. Voroshnin, O. J. Clark, J. Sánchez-Barriga, S. L. Bud'ko, R.-J. Slager, P. C. Canfield, and A. Kaminski, *Nature (London)* **603**, 610 (2022).
- [26] L.-L. Wang, J. Ahn, R.-J. Slager, Y. Kushnirenko, B. Ueland, A. Sapkota, B. Schruck, B. Kuthanazhi, R. McQueeney, P. Canfield *et al.*, [arXiv:2203.12541](https://arxiv.org/abs/2203.12541).
- [27] P. C. Canfield, T. Kong, U. S. Kaluarachchi, and N. H. Jo, *Philos. Mag.* **96**, 84 (2016).
- [28] P. C. Canfield, *Rep. Prog. Phys.* **83**, 016501 (2020).
- [29] R. Jiang, D. Mou, Y. Wu, L. Huang, C. D. McMillen, J. Kolis, H. G. Giesber III, J. J. Egan, and A. Kaminski, *Rev. Sci. Instrum.* **85**, 033902 (2014).
- [30] B. Kuthanazhi, N. H. Jo, L. Xiang, S. L. Bud'ko, and P. C. Canfield, *Philosophical Magazine*, **102**, 542 (2022).
- [31] A. P. Sakhya, P. L. Paulose, A. Thamizhavel, and K. Maiti, *Phys. Rev. Materials* **5**, 054201 (2021).
- [32] Y. Wu, D. Mou, N. H. Jo, K. Sun, L. Huang, S. L. Bud'ko, P. C. Canfield, and A. Kaminski, *Phys. Rev. B* **94**, 121113(R) (2016).
- [33] S.-Y. Xu, I. Belopolski, N. Alidoust, M. Neupane, G. Bian, C. Zhang, R. Sankar, G. Chang, Z. Yuan, C.-C. Lee *et al.*, *Science* **349**, 613 (2015).
- [34] L. Yang, Z. Liu, Y. Sun, H. Peng, H. Yang, T. Zhang, B. Zhou, Y. Zhang, Y. Guo, M. Rahn *et al.*, *Nat. Phys.* **11**, 728 (2015).
- [35] B. Q. Lv, H. M. Weng, B. B. Fu, X. P. Wang, H. Miao, J. Ma, P. Richard, X. C. Huang, L. X. Zhao, G. F. Chen, Z. Fang, X. Dai, T. Qian, and H. Ding, *Phys. Rev. X* **5**, 031013 (2015).
- [36] S.-Y. Xu, N. Alidoust, I. Belopolski, Z. Yuan, G. Bian, T.-R. Chang, H. Zheng, V. N. Strocov, D. S. Sanchez, G. Chang *et al.*, *Nat. Phys.* **11**, 748 (2015).